

Research Paper

R_e . II. Understanding (IC 3475)-type galaxy, aka ultra-diffuse galaxy, structural scaling relations

Alister W. Graham¹

¹ Centre for Astrophysics and Supercomputing, Swinburne University of Technology, Hawthorn, Victoria 3122, Australia.

Abstract

It is explained why ultra-diffuse galaxies (UDGs), a subset of (IC 3475)-type galaxies, do not have *unexpectedly* large sizes but large sizes that are in line with expectations from the *curved* size-luminosity relation defined by brighter early-type galaxies (ETGs). UDGs extend the faint end of the (absolute magnitude, \mathcal{M})-log(Sérsic index, n) and \mathcal{M} -(central surface brightness, μ_0) relations defined by ETGs, leading to the large effective half-light radii, R_e , in UDGs. It is detailed how the scatter in μ_0 , at a given \mathcal{M} , relates to variations in the galaxies' values of n and effective surface brightness, μ_e . These variations map into changes in R_e and produce the scatter about the \mathcal{M} - R_e relation at fixed \mathcal{M} . Similarly, the scatter in \mathcal{M} , at fixed μ_0 and n , can be mapped into changes in R_e . The increased scatter about the faint end of the \mathcal{M} - R_e relation and the smaller scatter about \mathcal{M} -(isophotal radii, R_{iso}) relations are explained. Artificial and potentially misleading size-luminosity relations for UDGs are also addressed. The suggestion that there may be two types of UDG appears ill-founded, arising from the scatter about the \mathcal{M} - μ_0 relation, which persists at all magnitudes. Hopefully, the understanding presented here will prove helpful for interpreting the many low surface brightness galaxies that the Large Synoptic Survey Telescope (LSST) will detect.

Keywords: galaxies: dwarf — galaxies: elliptical and lenticular, cD — galaxies: formation — galaxies: fundamental parameters — galaxies: structure.

(Received xx xx xxxx; revised xx xx xxxx; accepted xx xx xxxx)

1. Introduction

Reaves (1956) introduced the IC 3475 (I) galaxy type after he analysed the large low surface brightness (LSB) dwarf-mass early-type galaxy (ETG) IC 3475. Many such I-type galaxies, e.g. DDO 28 and DDO 29, were subsequently found in the David Dunlap Observatory dwarf galaxy catalogue once distances became available (Fisher & Tully 1975), and many other IC 3475 types were reported (e.g. Reaves 1983; Sandage & Binggeli 1984; Vigroux et al. 1986). As noted by Reaves (1983), these large LSB galaxies were designated by the letter 'I', encapsulating both "IC 3475" and, to a degree, also their (weakly) "Irregular" structure.^a Sandage & Binggeli (1984) noted that IC 3475 was a bright example of the huge [LSB] systems in their catalogue (Binggeli et al. 1985). In recent years, a subset of these large LSB galaxies has been referred to as ultra-diffuse galaxies (UDGs: Koda et al. 2015; van Dokkum et al. 2015) if their major-axis effective half-light radius, $R_{e,\text{maj}}$, is larger than ~ 1.5 kpc and their central B - or g -band surface brightness fainter than ≈ 24 mag arcsec⁻².

This study demonstrates how UDGs (and IC 3475 type galaxies) appear as the natural extension of dwarf early-type galaxies (dETGs) in key photometric scaling diagrams, with the dETGs known to be the extension of ordinary high surface brightness ETGs (Graham & Guzmán 2003; Graham 2019). UDGs, dETGs, and ordinary ETGs follow the same log-linear (absolute magnitude, \mathcal{M})-log(Sérsic index, n) and \mathcal{M} -(central surface brightness, μ_0) relations. In Graham (2023),

it was mentioned that the UDGs may also follow the same curved size-luminosity relation (Graham et al. 2006) as (dwarf and ordinary) ETGs, extending the sequence to fainter magnitudes (lower stellar masses) and larger R_e . Here, this prediction is shown and quantified. Graham (2019) explained how the value of \mathcal{M} associated with the bend in this size-luminosity relation depends on the arbitrary percentage of light enclosed within the scale radius, which is invariably set at 50 per cent to give R_e . Consequently, this bend does not signify a physical division or unique formation processes operating above and below this magnitude, and care needs to be taken when interpreting slopes in size-luminosity diagrams, especially when the sample selection further slices the data. Just as there is a continuity in structure between dETGs and ordinary ETGs, no distinct separation exists between UDGs and (dwarf and ordinary) ETGs in the \mathcal{M} - R_e diagram. Furthermore, this study reveals the reasons behind the increased scatter observed in the size-luminosity relation at faint magnitudes.

The data used for this presentation is described in Section 2, and the analysis is performed in Section 3, where the key results are presented. A review is provided in Section 4, along with a select discussion of some immediate and important implications and a recognition that the ETG sequence is one of mergers, from primaeval galaxies to wet-merger-built dust-rich S0 galaxies and dry-merger-built E galaxies.

2. Data

Two compilations of galaxy structural parameters have been used, one for (dwarf and ordinary) ETGs (Graham & Guzmán 2003) and one for UDGs (Buzzo et al. 2025).

Author for correspondence: A.W. Graham, Email: AGraham@swin.edu.au

Cite this article: Graham A.W. (2025) R_e . II. Understanding (IC 3475)-type galaxy, aka ultra-diffuse galaxy, structural scaling relations *Publications of the Astronomical Society of Australia* 00, xxx–xxx. <https://doi.org/10.1017/pasa.xxxx.xx>

^aUse of the letter 'I' also encapsulated the presence of some Population I stars.

The ETG sample comprises the alleged E galaxies from Caon et al. (1993), Faber et al. (1997, no Sérsic indices), Binggeli & Jerjen (1998), Stiavelli et al. (2001, R_e derived from the other Sérsic parameters), and the dETGs modelled in Graham & Guzmán (2003). The parameters displayed in this work pertain to the B -band on the Vega magnitude system and include the galaxies' absolute magnitude, \mathcal{M}_B , and the central surface brightness, $\mu_{0,B}$. For simplicity, no subscript B is assigned to the Sérsic index n or the effective half-light radii, R_e , although, due to radial colour gradients, these parameters are slightly dependent on the filter used (Kelvin et al. 2012; Häußler et al. 2013; Kennedy et al. 2016a,b).

The UDG sample consists of 36 'nearly UDGs' (NUDGs)^b presented in Buzzo et al. (2025), see also Marleau et al. (2024), plus their remodelled data for another 28 UDGs previously studied by Buzzo et al. (2022), along with data for another 59 UDGs taken from Buzzo et al. (2024). The NUDGs are regarded as mainly dE galaxies (Buzzo et al. 2025). The UDG and NUDG data compilation spans stellar masses of $7 \leq \log(M_\star/M_\odot) \leq 8.5$ dex, and their g -band data is used here. Given that the $g-z$ colours peak at $\approx 0.9-1$, this data is expected to have $g-i \approx 0.8 \pm 0.1$ and $B-V \approx 0.6 \pm 0.1$, and the g -band magnitudes are transformed into B -band magnitudes using $B = g + 0.35$ (Jester et al. 2005; Jordi et al. 2006), which should vary by only ± 0.04 mag given the colour spread in the data. The UDG and NUDG galaxies were separated into one of two classes (A or B) by Buzzo et al. (2025, see their section 4.3), based on an array of galaxy and associated globular cluster system properties.^c

As with the ETG sample, the most distant UDGs are located in the Coma cluster, which is ~ 100 Mpc distant. Given this proximity, the cosmological corrections^d are minor, and only the $(1+z)^4$ surface brightness dimming correction is applied.

3. Analysis and Relations

The data points in the left and central panel of Figure 1 reproduce the B -band (absolute magnitude, \mathcal{M}_B)–(central surface brightness, $\mu_{0,B}$) and \mathcal{M}_B –(Sérsic index, n) diagrams from Graham & Guzmán (2003, their Figure 9). The two empirical relations shown here are

$$\mathcal{M}_B = 0.63\mu_{0,B,\text{obs}} - 28.7, \sigma = 0.8 \text{ mag} \quad (1)$$

and

$$\mathcal{M}_B = -10.0 \log(n) - 14.0, \quad (2)$$

where σ denotes the 1-sigma scatter in the \mathcal{M}_B -direction about the \mathcal{M}_B – $\mu_{0,B}$ relation. These slopes and intercepts represent just a slight (5 per cent) variation on the values reported by Graham & Guzmán (2003). The subscript 'obs' has been added to $\mu_{0,B}$ to differentiate this observed surface brightness from an upcoming adjusted value.

The curved line in Figure 1c is not a fit to the data; it is the solution for Sérsic (1968a) $R^{1/n}$ light profiles (Capaccioli 1989; Graham & Driver 2005) based on Equations 1 and 2. This curve is for the radius equivalent to the geometric mean of the minor and major axis, $R_{e,\text{eq}}$, coming from the analytical expression

$$\mathcal{M} = \langle \mu \rangle_{e,\text{abs}} - 2.5 \log(2\pi R_{e,\text{eq}}^2) - 36.57, \quad (3)$$

with $\langle \mu \rangle_{e,\text{abs}}$ the absolute mean effective surface brightness and $R_{e,\text{eq}}$ in kpc (see Graham & Driver 2005, their Equation 12). As such,

$\langle \mu \rangle_{e,\text{abs}} = \langle \mu \rangle_e - 10 \log(1+z)$. Equation 3 can be re-expressed as

$$\log R_{e,\text{eq}}(\text{kpc}) = (\langle \mu \rangle_{e,\text{abs}} - \mathcal{M}_B)/5.0 - 7.713. \quad (4)$$

The difference between $\langle \mu \rangle_e$ and μ_0 (and $\langle \mu \rangle_{e,\text{abs}}$ and $\mu_{0,\text{abs}}$) is a (mathematical, not empirical) function of the Sérsic model, given by

$$\mu(R) = \mu_e + \frac{2.5b_n}{\ln(10)} \left[(R/R_e)^{1/n} - 1 \right], \quad (5)$$

and, in particular, the Sérsic index n , such that

$$\langle \mu \rangle_e = \mu_0 + 2.5b/\ln(10) - 2.5 \log[f(n)], \quad (6)$$

with the effective surface brightness at R_e denoted μ_e and

$$\mu_0 + 2.5b/\ln(10) = \mu_e \quad (7)$$

(see Equations 7, 8 and 9 from Graham & Driver 2005). One additionally has that

$$f(n) = \frac{ne^b \Gamma(2n)}{b^{2n}}, \quad (8)$$

with b a function of n obtained by solving $\gamma(2n, b)/\Gamma(2n) = 1/2$, and Γ is the complete gamma function.

Therefore, knowing how n and $\mu_{0,B}$ vary with \mathcal{M}_B (Equations 1 and 2), one knows how $\langle \mu \rangle_{e,B}$ (and μ_e) varies with \mathcal{M}_B , and hence, $R_{e,\text{eq}}$ can be derived as a function of \mathcal{M}_B . This derivation is shown by the curve in Figure 1c, explaining the trend in the data toward larger sizes at lower luminosities. Although this curved size-luminosity relation was presented in Graham et al. (2006) and Graham & Worley (2008), it is extended here to fainter magnitudes to show better the expected increase in size of fainter ETGs/UDGs.

The dashed lines in Figure 1a roughly capture the $\pm 2\sigma$ scatter. These lines have been combined with Equation 2 to produce the dashed curves in Figure 1c. They are insightful because they show how, for a fixed n and $\mu_{0,B}$, changes in luminosity are met by changes in size. This combination results in shifts roughly along the size-luminosity relation for galaxies with high Sérsic indices but perpendicular to it for galaxies with low Sérsic indices. At faint magnitudes, where the Sérsic index is low, a 2σ change in magnitude of 1.6 mag (or roughly a factor of 4 in luminosity) requires a roughly factor of 2 change in $R_{e,\text{eq}}$. This explains the broadening of the size-luminosity relation for ETGs at low masses.

Figure 2 introduces the UDGs, which appear to be the extension of (ordinary and dwarf) ETGs to fainter magnitudes. This is most immediately obvious in the \mathcal{M}_B – $\mu_{0,B}$ and \mathcal{M}_B – $\log(n)$ diagrams due to the roughly log-linear behaviour of these relations before the onset of core depletion in the massive elliptical galaxies built from gas-poor major mergers. The following slightly revised version of Equation 1 better matches the fuller ensemble of data shown in Figure 2a:

$$\mathcal{M}_B = 0.59\mu_{0,B,\text{obs}} - 28.1, \sigma = 0.8 \text{ mag}. \quad (9)$$

By feeding this empirical relation into Equations 4 and 6, one derives the following relation shown by the black curve in Figure 2c.

$$\log R_{e,\text{eq}}(\text{kpc}) = 0.139\mathcal{M}_B - 0.5 \log[f(n)] + 0.217b + 1.812, \quad (10)$$

with $n = 10^{-(14.0+\mathcal{M}_B)/10.0}$ coming from Equation 2.

It is noted that a sample collection gap is evident in Figure 2a at $\mathcal{M}_B > -12$ mag and $\mu_{0,B} < 24$ mag arcsec⁻², leading to a small triangular cutout that can be seen to propagate into Figure 2c (and Figure 3c). This creates the illusion of a trend for the UDGs and NUDGs in the \mathcal{M}_B – R_e diagram that is roughly perpendicular to the actual trend for UDGs/NUDGs and (dwarf and ordinary) ETGs. That is, Figure 2c reveals how the arbitrary sample selection of the UDGs yields an artificial and misleading size-luminosity relation.

^bThis term was coined by Forbes & Gannon (2024).

^cFor the sample from Buzzo et al. (2024), the class adopted here is that derived without the number of globular clusters used as a criterion; this was done as it resulted in a greater number of assigned classes.

^dThese are the K -correction, evolutionary correction, and $(1+z)^4$ surface brightness dimming.

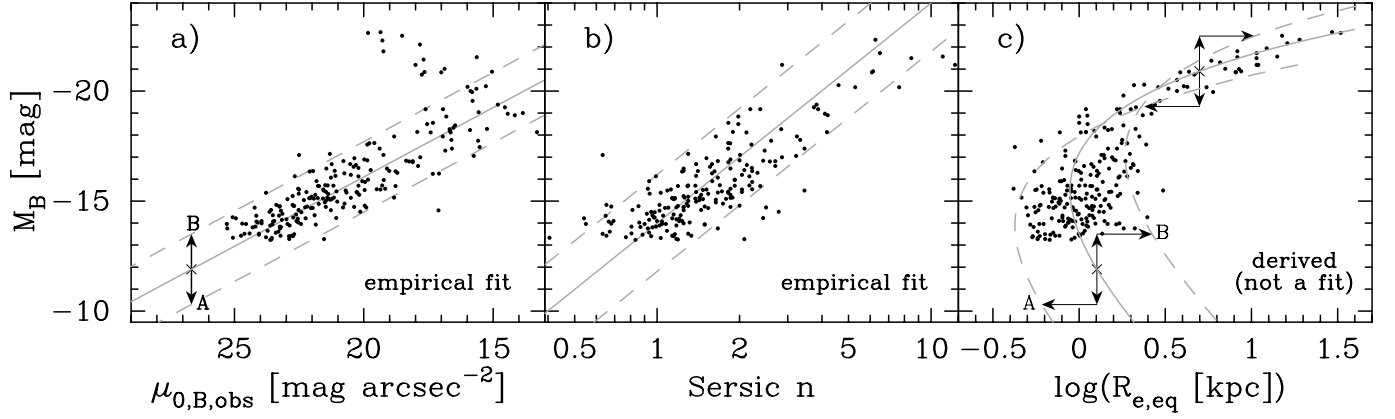


Figure 1. Absolute magnitude versus central surface brightness (Equation 1, panel a), Sérsic index (Equation 2, panel b), and (equivalent axis) effective half-light radius (Equation 4, panel c) for ETGs. Data from Graham & Guzmán (2003). The dashed lines in panel a) ensnare roughly the $\pm 2\sigma$ scatter, and they have been mapped into panel c). The arrows reveal how a change in absolute magnitude at fixed $\mu_{0,B}$ and n results in a corresponding change in R_e , simultaneously explaining the low and high levels of scatter at bright and faint absolute magnitudes, respectively. For the modelled lines in panel c), the central surface brightness (and Sérsic index) associated with points A and B are the same, but R_e is different because the magnitude is different (see Equation 4).

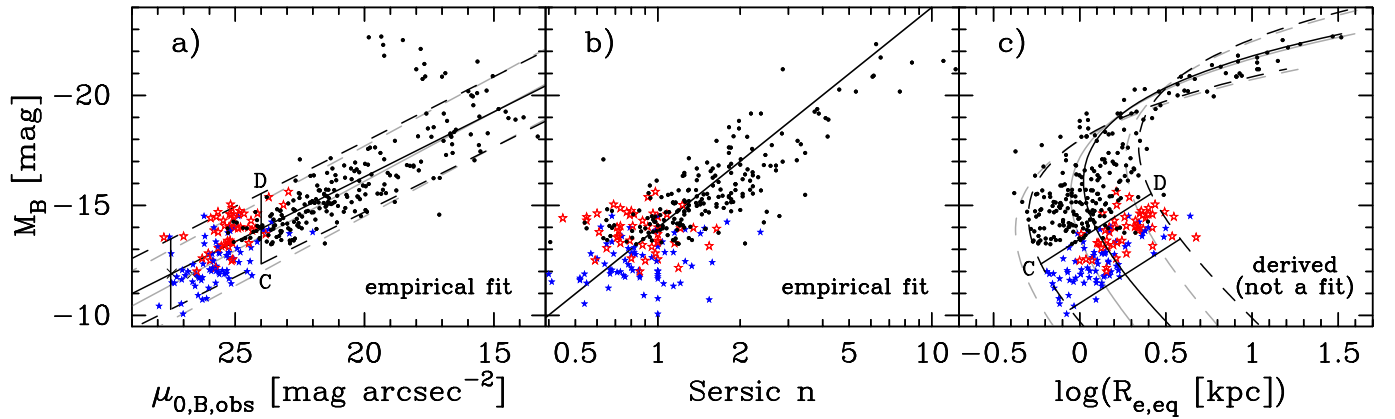


Figure 2. Extension of Figure 1 with the addition of UDG and NUDG data from Buzzo et al. (2025) and Buzzo et al. (2024), and a slightly revised $\mathcal{M}_B - \mu_{0,B,obs}$ relation (Equation 9) and thus a slightly revised $\mathcal{M}_B - R_{e,eq}$ relation (Equation 10). The colour-coding tracks the two classes (A=blue filled star, B=red open star) assigned to the UDGs and ‘NUDGs’ by Buzzo et al. (2025). The two vertical lines of constant central surface brightness shown in the lower left of panel a) map into the diagonal lines seen in panel c), with the arrows in Figure 1c revealing how this is done. This reveals and explains the creation of a misleading size-luminosity relation for UDGs.

3.1. Major axis radii

If one uses the major axis radius, $R_{e,maj} (= R_{e,eq} \sqrt{b/a})$, where b/a is the minor-to-major axis ratio), in the size-luminosity diagram, then an adjustment to Figure 2a is required. Due to an increased size, a fainter surface brightness is required to balance the derivation of the magnitude (Equation 3). The adjusted surface brightness affects $\langle \mu \rangle_e$ and μ_0 equally and is given by

$$\mu_{0,B,adj} = \mu_{0,B,obs} - 2.5 \log(b/a). \quad (11)$$

This is similar to a correction for disc galaxies where $b/a \approx \cos(i)$ and i is the inclination of the disc such that $i=0$ denotes alignment of the galaxy’s polar axis with our line of sight, i.e. face-on. Although rotation and the presence of faint spiral patterns and bars in some dwarf galaxies reveal their disc-like nature, most are thought to be triaxial, and the brighter dETGs with regular isophotes are less triaxial and slightly more spherical (e.g. Sung et al. 1998). Basically, the rebalancing performed through Equation 3 accounts for the larger radii ($R_{e,maj} > R_{e,eq}$) encapturing a fainter ‘mean effective surface brightness’, which is implemented here by making the central surface brightness fainter via Equation 11.

Observed axis ratios for the dETG sample in Binggeli & Jerjen (1998) have come from the values reported by Binggeli & Cameron (1993), while for the remaining UDG/NUDG and (dwarf and ordinary) ETG samples, they have come from the reported ratios or ellipticities in their respective papers. The result is shown in Figure 3a, along with the slightly revised line

$$\mathcal{M}_B = 0.59\mu_{0,B,adj} - 28.4, \sigma = 0.8 \text{ mag}, \quad (12)$$

and thus a new expression for the $\mathcal{M}_B - R_{e,maj}$ curve (Figure 3c) that differs slightly from Equation 10 shown in Figure 2c. This new equation for the major axis R_e is given by

$$\log R_{e,maj}(\text{kpc}) = 0.139\mathcal{M}_B - 0.5 \log[f(n)] + 0.217b + 1.914. \quad (13)$$

3.2. Min(d)ing the scatter

Dry major mergers between ETGs containing supermassive black holes can scour away the core of the newly-formed galaxy, producing the abrupt turn in the $\mathcal{M}_B - \mu_{0,B}$ relation at $\mathcal{M}_B \approx -20.5$ mag (Graham & Guzmán 2003) rather than at the previously suggested $\mathcal{M}_B \approx -18$ mag (Kormendy 1985; Faber et al. 1997, see their discussion of their

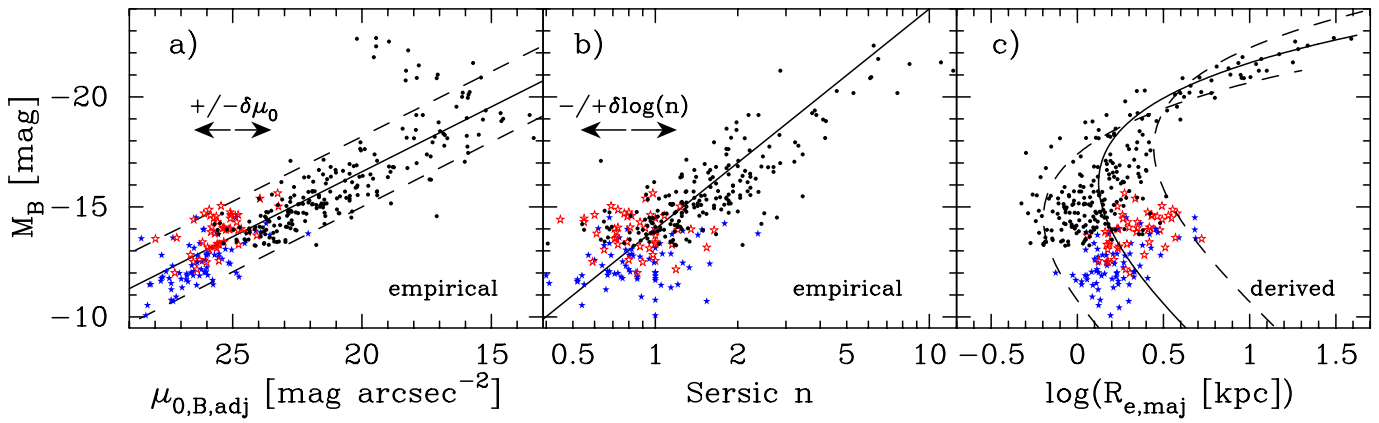


Figure 3. Variant of Figure 2 showing $\mu_{0,B,\text{adj}}$ (see Equations 11 and 12) in panel a) and $R_{e,\text{maj}}$ (see Equation 13) in panel c). At fixed \mathfrak{M}_B , the (horizontal) scatter $\delta\mu_{0,B}$ is directly related to the scatter $\delta\log(n)$ (panel b) and $\delta\mu_{e,B}$ (see Figure 4).

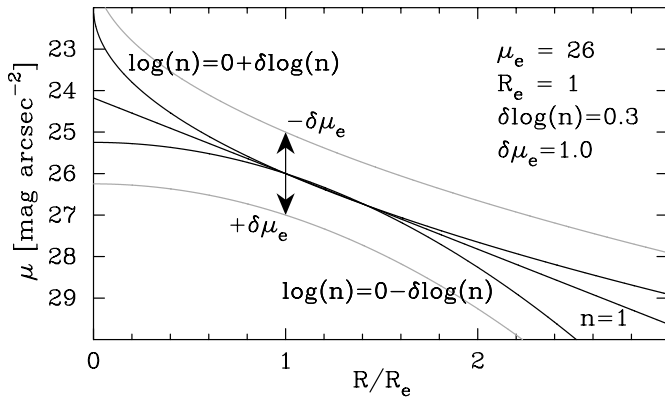


Figure 4. An example of how variations/offsets in μ_e and n for a surface brightness profile will result in the offset to μ_0 . For a given \mathfrak{M} , with an associated μ_0 and n from the $\mathfrak{M}-\mu_0$ and $\mathfrak{M}-\log(n)$ relations, the horizontal offsets $\delta\mu_0$ seen in Figures 1a–3a are attributable to the offsets $\delta\mu_e$ and $\delta\log(n)$.

Figure 4c based on the nucleated and stripped galaxy M32). Graham & Sahu (2023) suggested that extensive scouring from the multiple mergers (aided by captured satellites: Goerdt et al. 2010; Bonfini et al. 2015) that build brightest cluster galaxies, typically massive ETGs, leads to such a dramatic redistribution of stars that the galaxy’s reduced central concentration and stellar build-up at larger galactic radii changes the galaxy profile from having an obvious core, and thus a core-Sérsic light profile, to a low- n Sérsic profile that may additionally have an exponential-like envelope (e.g. Seigar et al. 2007). This transformation was termed ‘galforming’. While this explains large-scale departures of E galaxies at high masses from the $\mathfrak{M}_B-\mu_{0,B}$ and $\mathfrak{M}_B-\log(n)$ relations, the scatter about these relations can be mined for insight into the formation and evolution of ETGs. As displayed in Figure 3, $\delta\mu_{0,B}$ and $\delta\log(n)$ shall denote the horizontal scatter/offset between the data and the ‘expected’ value (from the $\mathfrak{M}_B-\mu_{0,B}$ and $\mathfrak{M}_B-\log(n)$ relations) at the same magnitude.

One can deduce a lot from coupling the $\mathfrak{M}_B-\mu_{0,B}$ and $\mathfrak{M}_B-\log(n)$ relations with the properties of the 3-parameter Sérsic model used to describe ETG light profiles. The previous section showed how \mathfrak{M}_B , $\mu_{0,B}$, and n dictate the value of R_e and $\langle\mu\rangle_{e,B}$ (and $\mu_{e,B}$). Conversely, R_e , $\mu_{0,B}$ (or $\langle\mu\rangle_{e,B}$ or $\mu_{e,B}$), and n yielded the value of \mathfrak{M}_B for a given Sérsic light profile. Here, it is revealed how the scatter about the \mathfrak{M}_B-R_e relation can be traced back to the scatter about the $\mathfrak{M}_B-\mu_{0,B}$

relation, which is directly related to the galaxies’ variation in both $\mu_{e,B}$ and n at a given magnitude (see Figure 4).

Equation 3 reveals that, in a sense, a galaxy’s values of \mathfrak{M} and R_e depend on its value of $\langle\mu\rangle_e$, and Equation 6 shows how $\langle\mu\rangle_e$ depends on μ_e and n . Therefore, for a given \mathfrak{M} , the value of R_e depends on μ_e and n . Consequently, at a given \mathfrak{M} , the scatter about the $\mathfrak{M}-R_e$ curve relates to the scatter in μ_e and n about their median expected value, as traced by the $\mathfrak{M}-\mu_e$ and $\mathfrak{M}-\log(n)$ relations. The latter horizontal scatter is seen in the $\mathfrak{M}-\log(n)$ diagram (Figure 3b), while the former horizontal scatter is displayed in Figure 6.

For each galaxy, with its observed values of \mathfrak{M}_B and n , one additionally has the expected value of n from the $\mathfrak{M}_B-\log(n)$ relation. One can then calculate $\mu_{0,B} - \mu_{e,B}$ for each of these two values of n (Equation 7) in order to explore how the difference/offset in the Sérsic index, $\delta\log(n)$, propagates into a horizontal offset of central surface brightness about the $\mathfrak{M}_B-\mu_{0,B}$ relation. The remaining scatter about the $\mathfrak{M}_B-\mu_{0,B}$ relation is due to the difference between the expected value of $\mu_{e,B}$ (based on the expected values of $\mu_{0,B}$ and n for any \mathfrak{M}_B) and the observed value of $\mu_{e,B}$. These offsets are denoted $\delta\mu_e$, with an example illustrated in Figure 4 using $n = 1$ and $\mu_e = 26 \text{ mag arcsec}^{-2}$ as the ‘expected’ values. From Figure 4, one can envisage how changes to n and μ_e alter μ_0 .

Figure 5a reveals that, for a given \mathfrak{M}_B , UDGs with a brighter $\mu_{0,B}$ than ‘expected’ (from the $\mathfrak{M}_B-\mu_{0,B}$ relation) also have a higher value of n (than expected from the $\mathfrak{M}_B-\log(n)$ relation). In contrast, those with a fainter-than-expected value of $\mu_{0,B}$ have a lower-than-expected value of n for their absolute magnitude. This change in the Sérsic index accounts for some of the horizontal scatter in the $\mathfrak{M}_B-\mu_{0,B}$ diagram, as shown in Figure 5b. The offset in $\mu_{0,B}$ due to the differences between the observed and expected values of n is given by $(2.5/\ln(10))[b_{\text{obs}} - b_{\text{expected}}]$, with $b \approx 1.9992n - 0.3271$, for $0.5 < n < 10$ (Capaccioli 1989). Figure 5b also reveals that, for UDGs with their small Sérsic indices, the offset in the observed value of n from the expected value accounts for about one-third of the UDGs’ offset between the observed value of $\mu_{0,B}$ and the expected value at that magnitude. For brighter ETGs, with their larger values of n , the difference between the observed and expected value of n accounts for most of their scatter about the $\mathfrak{M}_B-\mu_{0,B}$ relation. This is as expected given how the difference between μ_e and μ_0 in the $R^{1/n}$ model increases roughly linearly with the Sérsic index while, and this is the key, the logarithmic scatter $\delta\log(n)$ about the $\mathfrak{M}_B-\log(n)$ relation does not sufficiently decline as n increases. That is, the horizontal scatter δn about the $\mathfrak{M}_B-\log(n)$ relation increases with increasing n .

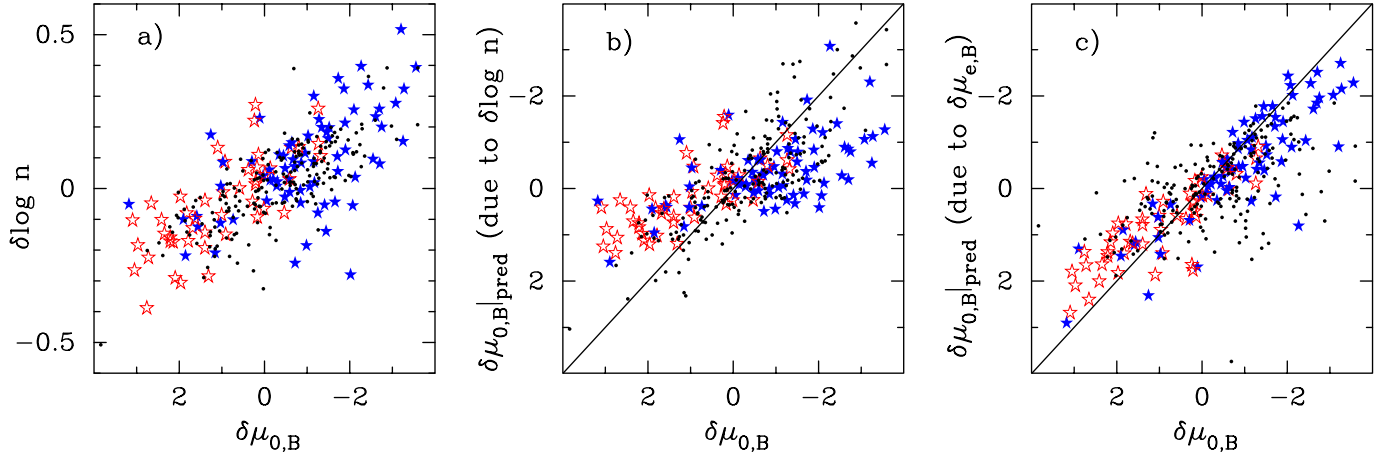


Figure 5. Breaking down the scatter in the \mathcal{M}_B - $\mu_{0,B}$ diagram for ETGs. At fixed \mathcal{M}_B , the horizontal scatter $\delta\mu_{0,B}$ and $\delta\log(n)$ from Figures 2a) and 2b) are shown against each other in panel a). The predictable contribution to $\delta\mu_{0,B}$ arises from offsets in $\log(n)$ and $\mu_{e,B}$ from their expected values (based on the scaling relations). These are shown in panels b) and c), respectively. The different behaviour of the UDGs from the (dwarf and ordinary) ETGs is explained in Section 3.2 and simply reflects their different Sérsic indices.

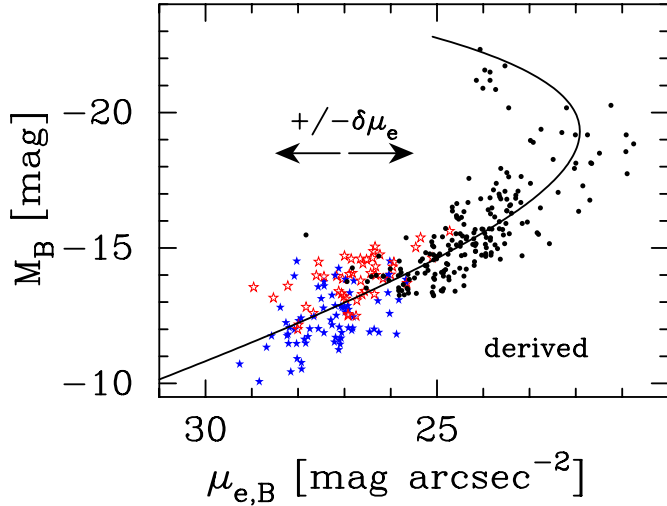


Figure 6. Effective surface brightness, $\mu_{e,B}$, at R_e versus \mathcal{M}_B . The curve is not a fit but instead a derivation from the \mathcal{M}_B - μ_0 and \mathcal{M}_B - $\log(n)$ relations (Equations 9 and 2).

The difference between the observed value of $\mu_{e,B}$ and the expected value at each magnitude (Figure 6) accounts for the remaining offset of the observed value of $\mu_{0,B}$ from the expected value of $\mu_{0,B}$ at that magnitude, i.e. the scatter. This component of the difference in $\mu_{0,B}$ is shown in Figure 5c, where it can be seen that differences in $\mu_{e,B}$ dominate the difference in $\mu_{0,B}$ for the UDGs. For the (brighter) ETGs, the contribution to the scatter about the \mathcal{M}_B - $\mu_{0,B}$ relation stemming from the different $\mu_{e,B}$ values at a given \mathcal{M}_B is seen to be sub-dominant to the scatter arising from the difference between their observed and expected Sérsic index.

In essence, the situation for the UDGs can be summarised as follows. UDGs with $\mu_{0,B}$ values fainter than expected for their magnitude (based on the \mathcal{M}_B - $\mu_{0,B}$ relation) and with Sérsic indices smaller than expected (based on the \mathcal{M}_B - $\log(n)$ relation) will have effective half-light radii that are larger than expected, where ‘expected’ means the value coming from the \mathcal{M}_B - $\mu_{0,B}$ and \mathcal{M}_B - $\log(n)$ relations. Equally, UDGs with brighter than expected μ_0 values and larger than expected n values will have smaller than expected R_e values. These shifts (in

R_e) from expectation come on top of the curved \mathcal{M}_B - R_e relation for ETGs, of which UDGs are a part.

3.2.1. Ellipticity

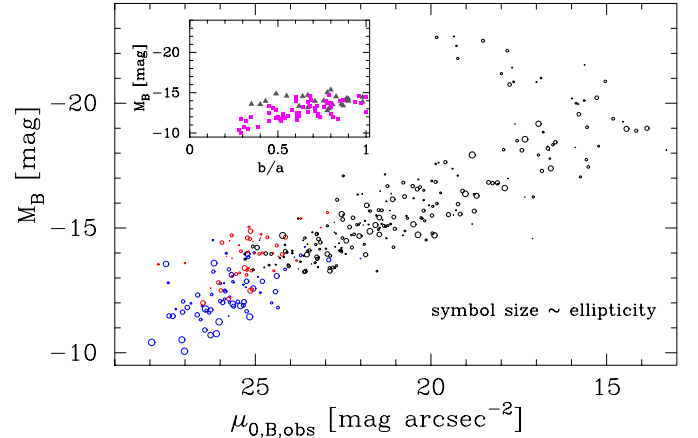


Figure 7. Variant of Figure 2a, in which the symbol size is now proportional to the ellipticity ($= 1 - b/a$) such that galaxies that appear round have a small symbol size. In the inset panel, the grey triangles represent 28 UDGs predominantly in clusters, while the pink squares represent 59 UDGs in low-to-moderate density environments. UDGs with high b/a ratios are prevalent in both environments and are thus not a product of the environment. At faint absolute magnitudes, the samples’ b/a ratios are small, possibly a result of sample selection (see the discussion in Section 3.2.1).

A factor that could contribute to some of the horizontal scatter about the \mathcal{M}_B - $\mu_{0,B}$ relation is the line-of-sight through the ETGs, with longer sight lines potentially leading to brighter surface brightnesses. It is important to understand that this can arise in two distinct ways. If the (dust-free) ETGs are oblate or disk-like, then those ETGs viewed with a more edge-on orientation will appear to have higher ellipticities and brighter surface brightnesses. As such, one would expect to find a predominance of low b/a galaxies occupying the right-hand side (high surface brightness side) of the \mathcal{M}_B - $\mu_{0,B}$ distribution. If, on the other hand, ETGs are more prolate, with one long axis and two shorter axes, then the sightline depth through these galaxies will be greatest when the long axis aligns with our line-of-sight and the

b/a axis ratio is highest. Conversely, their surface brightness will be faintest when they appear most elongated, i.e. higher ellipticity. Figure 7 displays the ellipticity of the ETGs. There is no obvious trend for high-ellipticity galaxies to occupy either the left or right side of the \mathcal{M}_B - $\mu_{0,B}$ distribution.

Cluster dETGs might be vertically-heated discs, which need not have ever hosted a spiral pattern. Should clusters be harassing disc galaxies to make them smaller and more ellipsoidal (Moore et al. 1996), then the effect should be greater on the lower mass systems and, thus, there should be a difference between the mean ellipticity of field and cluster UDGs of the same absolute magnitude. Rong et al. (2020) reported that UDGs near the centres of clusters are rounder than those near the outskirts, but those near the outskirts were also fainter, thus convoluting any attribution to an environmental effect because this \mathcal{M} - ϵ trend is also seen with UDGs not in clusters (Figure 7).

Buzzo et al. (2025) report that the sample of 59 UDGs from Buzzo et al. (2024) reside in low-to-moderate density environments, whereas galaxies in clusters heavily dominate the remodelled sample from Buzzo et al. (2022). The inset panel in Figure 7 shows the range of observed b/a axis ratios for these two UDG samples. It is informative. There is no clear environmental dependence. High b/a values are observed in the field and cluster ETGs, ruling out an environmental driver for these shapes. What is also apparent is that at faint magnitudes, the ratios are low, that is, at faint magnitudes the ellipticity is high. If these are oblate disc-like galaxies at faint magnitudes, then some of this population should have a relatively face-on orientation and high b/a ratio. Given the lack of such detections, it seems plausible that sample selection effects are at play such that at these faint magnitudes, only systems whose surface brightness has been enhanced by an increased line-of-sight depth have made it into the sample. Finally, if ordered rotation had produced oblate discs in the UDGs, impeding their initial gravitational collapse and resulting in larger sizes, then the larger UDGs would be associated with a more elliptical, rather than round, population, which is not observed.

In conclusion, the apparent ellipticity may contribute to some scatter, but it does not produce strong trends in the present \mathcal{M}_B - $\mu_{0,B}$ diagram. It is, however, noted that the brighter S0 galaxies with rather edge-on discs and thus higher ellipticity may have been filtered from the sample because, in the past, they were more readily identified as disc galaxies rather than elliptical galaxies. Dwarf mass ($M_{\star, \text{gal}}/M_{\odot} \approx (2-5) \times 10^9$, $\mathcal{M}_B \approx -17.5 \pm 0.5$ mag) ETGs in clusters have the same kinematic properties as those in isolated field environments (Janz et al. 2017). This further undermines the notion that cluster-related processes have had a strong hand in shaping dETGs, implying that they are born as they are rather than transformed. This was the conclusion reached by Vigroux et al. (1986) in the case of IC 3475.

3.3. Isophotal radii

As seen in, for example, Forbes et al. (2008, their Figure 3) and Schombert & McGaugh (2014, their Figure 1), faint isophotal radii yield a tight \mathcal{M}_B -(isophotal radius, R_{iso}) relation. It has less scatter than the curved \mathcal{M}_B - R_e relation (e.g. Graham et al. 2006). This is explained here.

First, the \mathcal{M}_B - $\mu_{0,B}$ and \mathcal{M}_B - $\log(n)$ relations (Equations 9 and 2) are used to create five representative light profiles of the ETGs and UDGs with values of $n = 0.5, 1, 2, 4$, and 8 . The thick curves in Figure 8 show these profiles, and their $\mu_{e,B}$ and R_e values are marked with a star. Joining these stars traces out the curved $\mu_{e,B}$ - R_e relation for ETGs and UDGs. Next, accompanying each of these five light profiles are two offset profiles with the same \mathcal{M}_B . One has had $\delta \log(n) = 0.2$ dex and $\delta \mu_e = -1.5$ mag arcsec $^{-2}$ applied, while the other has had $\delta \log(n) =$

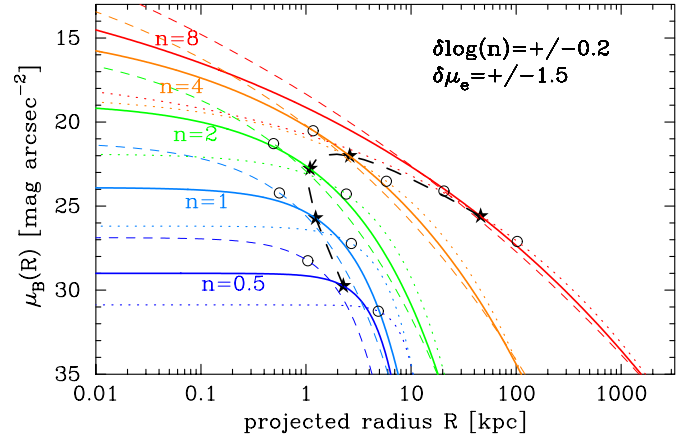


Figure 8. Five representative B -band light profiles of ETGs with different Sérsic indices are shown (thick solid curves). For each value of n , an associated absolute magnitude and central surface brightness are assigned from Equations 2 and 9, from which the effective surface brightness and radius can then be calculated (Equation 10). For each profile, the ‘effective’ parameters $\mu_{e,B}$ and R_e are shown by the stars, and the dashed curve connecting them traces the $\mu_{e,B}$ - R_e relation for ETGs. While keeping the absolute magnitude fixed, offsets of $\delta \mu_e = \pm 1.5$ mag arcsec $^{-2}$ and $\delta \log(n) = \pm 0.2$ dex are applied to each profile, thereby generating offsets in $\mu_{0,B}$. This produces the dotted and dashed curves, whose μ_e and R_e values are shown by the open circles. These offset profiles yield slight differences in the isophotal radii relative to the larger changes seen in R_e , provided the chosen isophotal surface brightness is not too close to the light profile’s central surface brightness.

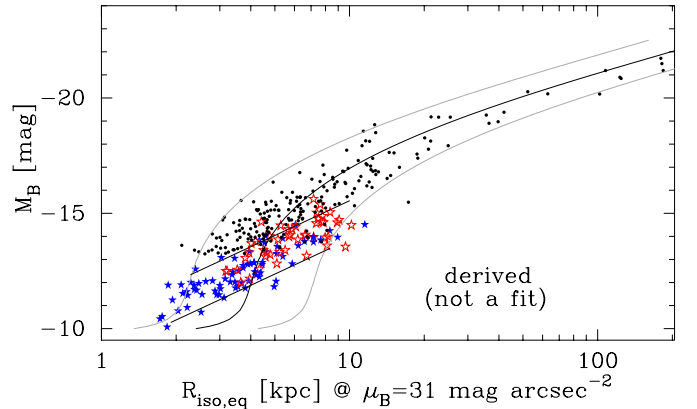


Figure 9. Absolute magnitude versus the ‘equivalent axis’ isophotal radius at $\mu_B = 31$ mag obtained from each galaxy’s Sérsic profile. The central black curve is derived using Equations 2 and 9, while the outer grey curves denote a ± 0.25 dex offset in isophotal radius at fixed \mathcal{M}_B . The two diagonal lines pertain to a fixed B -band central surface brightness of 24 and 27.5 mag arcsec $^{-2}$ and reveal how R_{iso} changes if \mathcal{M}_B changes by up to ± 1.6 mag while the associated Sérsic index is held fixed (at $n = 0.986$ and 0.613 , respectively).

-0.2 dex and $\delta \mu_e = +1.5$ mag arcsec $^{-2}$ applied. Their values of $\mu_{e,B}$ and R_e values are marked with an open circle. For each of the five cases, one can immediately see that the change to the isophotal radii from these perturbations is smaller than the change to R_e . That is the scatter at fixed \mathcal{M}_B about the \mathcal{M}_B - $\mu_{0,B}$ (and \mathcal{M}_B - $\log(n)$) relations will create a larger scatter about the \mathcal{M}_B - R_e relation (Figure 2c) than it will about an \mathcal{M}_B - R_{iso} relation (unless the isophotal level is close to the central surface brightness of the light profile).

The \mathcal{M}_B - $\mu_{0,B}$ and \mathcal{M}_B - $\log(n)$ relations have been used to derive the ‘expected’ isophotal radius at $\mu_B = 31$ mag arcsec $^{-2}$ for other values of n and \mathcal{M}_B , and this is shown in Figure 9 by the thick curve. For each galaxy from the data samples, their Sérsic parameters have

been used to compute the radius where $\mu = 31 \text{ mag arcsec}^{-2}$, which is also displayed in Figure 9. Where galaxies actually end is a separate topic (Shull 2014). The scatter in the data about the $\mathcal{M}_B-R_{\text{iso}}$ curve is small compared to that of the \mathcal{M}_B-R_e curve. As with Figure 2c, two diagonal lines of constant central surface brightness have been added to illustrate how the UDG/NUDG sample selection again results in a misleading luminosity-size relation at odds with that (the thick curved line) from its parent sample. Clearly, considerable care is needed when interpreting $\mathcal{M}_B-R_{\text{iso}}$ diagrams for UDGs.

4. Discussion

4.1. Division of ETGs

The notion that there may be two distinct (dwarf and ordinary) types of ETG was perhaps first raised by Sérsic (1968b) upon inspecting the departure of the fainter ETGs from the \mathcal{M}_B-R_e relation defined by the brighter ETGs. This departure is also seen in the $\mathcal{M}_B-\langle\mu\rangle_{e,B}$ diagram (e.g. Sandage et al. 1985, their Figure 3) and the $\mathcal{M}_B-\mu_e$ diagram (Figure 5). However, as detailed in Graham (2019), these departures (and departures in all diagrams involving ‘effective’ half-light parameters) arise from the systematically varying – with absolute magnitude – Sérsic (1968a) $R^{1/n}$ nature of their stellar distribution. The suggestion of a third (UDG) type of ETG due to their deviation to increasing sizes at yet fainter magnitudes in the \mathcal{M}_B-R_e diagram is dispelled here because bends in diagrams involving effective half-light parameters should not be used as a diagnostic tool for galaxy formation. As Graham (2019) explained, the magnitude associated with the ‘bend point’ in diagrams involving ‘effective’ parameters changes with the enclosed fraction of light used to define the ‘effective’ parameters. This voids any physical significance of the bend point in terms of galaxy formation scenarios.

There are, however, subtypes among the ETGs, which has undoubtedly added to the confusion when interpreting scaling relations involving effective half-light parameters. These subtypes are presented in Graham (2023) and encompass primordial/primaeval lenticular (S0) galaxies — including the UDGs at the faint end — that need not have once been spiral galaxies, plus major-merger-built S0 galaxies, which are dust-rich if a spiral galaxy was involved in the collision, elliptical (E) galaxies with fully embedded discs, and discless elliptical (E) galaxies. Therefore, the dwarf-mass ETGs are not simply small versions of giant S0 or E galaxies in that they represent an earlier stage of evolution. This aspect has likely muddled the waters and given false support to interpretations of a division at $\mathcal{M}_B \approx -18$ mag based on scaling diagrams involving μ_e , $\langle\mu\rangle_e$, and R_e .

The yet further division of UDGs and NUDGs into two classes by Buzzo et al. (2025) can be seen in Figure 2. It is immediately apparent that Class B (denoted by the open stars) is, on average, brighter than Class A (denoted by the filled stars). Therefore, the more massive Class B will have, on average, redder colours, given the colour-magnitude relation for dETGs (e.g. de Vaucouleurs & de Vaucouleurs 1972; Forbes et al. 2008; Graham 2024a). The redder colours will equate to a higher (stellar mass)-to-light ratio, M_*/L , for Class B, given the well-known M_*/L -colour trends (e.g. Bell & de Jong 2001). Class B will also have higher velocity dispersions, σ , given the luminosity- σ relation for dETGs (e.g. Davies et al. 1983; Toloba et al. 2014). Furthermore, Figure 2 reveals why the galaxies in Class B have larger sizes and, therefore, higher inferred total masses when using $\sigma^2 R_e/G$ as a proxy for dynamical mass. Consequently, Class B will have more globular clusters, given how this scales with the inferred halo mass (Spitler & Forbes 2009). To summarise, a division among UDGs (and NUDGs) indirectly but heavily based on

their distribution about the $\mathcal{M}_B-\mu_{0,B}$ relation will explain the offsets between the mean value of many parameters for Class A and B. This need not imply a second uniquely different origin story (e.g. ‘puffy dwarfs’: Errani et al. 2015; Conselice 2018) for LSB ETGs unless one is to attribute the scatter about the $\mathcal{M}_B-\mu_{0,B}$ relation to different formation scenarios.

The question of whether studies have identified two classes of UDG on either side of the $\mathcal{M}_B-\mu_{0,B}$ relation or whether the effect of intrinsic scatter on the scaling relations has been missed appears to have been answered in Section 3. A greater level of spin, i.e. ordered rotation, does not appear to correlate with the larger UDGs. Given that galaxies with a higher spin would be supported by rotation, in addition to velocity dispersion, one would expect them to be relatively flatter systems. However, the larger UDGs, which reside on the fainter central surface brightness side of the $\mathcal{M}_B-\mu_{0,B}$ relation, do not have smaller axis ratios (Figure 7). Equally, if there is a population of UDGs with edge-on discs yielding brightened μ_0 values, Figure 2c (and 3c) require them to have *smaller* radii (both R_{eq} and R_{maj}) than the other UDGs of the same magnitude. This is not observed; that is, they are not spun out to larger radii. What makes the first option even more problematic is that the scenario to preferentially place those UDGs assumed to have ‘puffed up’ after gas loss from stellar winds or ram pressure stripping (Saito 1979; Dekel & Silk 1986; Vader 1986; Di Cintio et al. 2017) on one side of the $\mathcal{M}_B-\mu_{0,B}$ relation seems unlikely to preferentially operate on the higher mass UDGs that are more capable of retaining their gas. One might expect that the proposed processes to ‘puff up’ some UDGs should preferentially operate on fainter, lower mass systems, yet the brighter, higher mass UDGs have the larger sizes. This undermines the relevance of this proposed additional formation scenario. Furthermore, the observed size-luminosity trend is readily explained because brighter galaxies require larger sizes (Equation 4) for a given Sérsic profile with fixed values of $\mu_{0,B}$ and n . That is, no recourse to different formation scenarios is required to explain the increased sizes or many of the trends observed in UDG properties that can be traced back to their differing mass.

Due to the ~ 3.2 mag of vertical scatter (± 2 -sigma) about the $\mathcal{M}_B-\mu_{0,B}$ relation, selecting a sample of LSB ETGs with $24 < \mu_{0,B} < 27.5$ mag arcsec $^{-2}$ results in an \mathcal{M}_B-R_e distribution that is roughly orthogonal to the wholesale \mathcal{M}_B-R_e correlation for ETGs (Figures 2c and 3c). This behaviour is also somewhat true for the $\mathcal{M}_B-R_{\text{iso}}$ relation (Figure 9). As Sung et al. (1998) noted, these misleading trends of brighter luminosities and larger sizes for samples with (a small range in) low central surface brightness had previously been used to separate LSB dwarf galaxies from blue compact dwarf galaxies.

As seen, faint galaxies with fainter surface brightnesses than other galaxies of the same faint magnitude have larger radii than those of the same faint magnitude. What causes this is unclear, although it is noted that those with larger radii also have smaller Sérsic indices. Rather than subsequently being puffed up after formation, these large galaxies may initially form this way. The ETG sequence may well be a primordial and merger-built sequence representing the long side of the Triangal (Graham 2023), encapsulating primaeval galaxies (UDG/IC 3475, dS0, dE), merger-built S0 galaxies, and multiple-merger-built E galaxies, with mass and Sérsic index increasing through mergers. This notion will be detailed further in a follow-up paper involving kinematical information. While there are several facets and intricacies to this problem, a broad overview is presented in Figure 10. It shows how the arbitrary and artificial division of LSB galaxies and regular-size dwarf-mass galaxies will result in a different average dynamical mass for each subdivision. The brighter dETGs galaxies have higher velocity dispersions due to the $\mathcal{M}_B-\sigma$

relation, and those with larger R_e values will have bigger dynamical masses when using $\sigma^2 R_e/G$ as a total mass indicator, and thus they will also have richer globular cluster systems (Spitler & Forbes 2009). However, they all belong to the ETG population with a continuous range of properties. Intrinsic scatter about the $\mathcal{M}_B - \mu_{0,B}$ and $\mathcal{M}_B - n$ scaling relations will be addressed in terms of dark matter fractions in a follow-up paper.

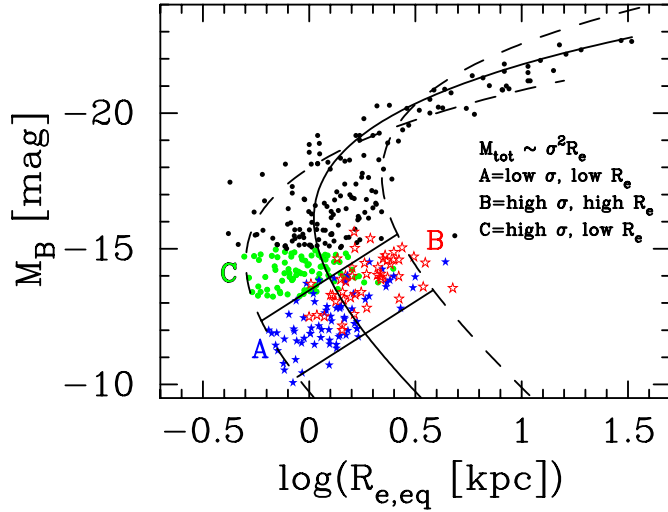


Figure 10. Given $\mathcal{M}_B \propto \sigma^2$ for dETGs (Davies et al. 1983; Graham 2013, and references therein), one can appreciate how the scatter about the $\mathcal{M}_B - R_e$ relation, shown here, results in different dynamical masses ($\sigma^2 R_e/G$), and in turn, mass-dependent trends, that are subject to arbitrary divisions of the dETG (including UDG) sample. The green dots are ETGs not in the UDG sample but with $\mathcal{M}_B \geq -15$ mag.

Although Amorisco & Loeb (2016) did not explore if their model for creating UDGs with larger R_e due to a larger angular momentum reproduces the $\mathcal{M}_B - \log(n)$ relation for ETGs^e, their conclusion that UDGs need not be shaped by their environment and that they are the natural extension of ordinary and dwarf ETGs agrees with this manuscript’s alternate analysis of the situation. The combination of lower n and fainter $\mu_{0,B}$ for a given absolute magnitude will result in a larger R_e (Section 3). This differs somewhat from the statement by Amorisco & Loeb (2016) that “the UDG population represents the tail of galaxies formed in dwarf-sized haloes with higher-than-average angular momentum”. If true, this would necessitate that, at fixed \mathcal{M}_B , the Sérsic index is lower (higher) for UDGs with higher (lower) angular momentum. This notion will be pursued in a follow-up paper.

It is hoped that the insight presented herein will aid studies of LSB galaxies made with the Large Synoptic Survey Telescope (LSST)^f, which is expected to start producing science-quality data this year. LSST is designed to explore the Universe with unprecedented depth in surface brightness. Placing discoveries in the LSB Universe in the proper context relative to HSB peers is essential for a holistic understanding.

^eWhile Amorisco & Loeb (2016) refer to models having different ‘concentrations’, they are not referring to a different radial concentration of stars as per the Sérsic model (Trujillo et al. 2001; Graham et al. 2001) but to a measure of the density contrast of the halo relative to the average background density of the Universe.

^f<https://www.lsst.org/>

4.2. Might they be discs?

The stellar discs in many local HSB ETGs (e.g. Capaccioli 1990; Rix & White 1990) went overlooked for decades, with Graham et al. (1998) concluding that the number of (discless) E galaxies is much lower than previously thought. This finding supported the view that low-luminosity^g ETGs are S0 galaxies (van den Bergh 1990). With increased numbers of kinematic maps, it is now known that among galaxies that are more massive than $\sim 10^9 M_\odot$, true pressure-supported E galaxies are only found at the high mass end ($\geq 10^{11} M_\odot$; Emsellem et al. 2011; Krajnović et al. 2013). These systems are built from the merger and summation of many disc galaxies (Graham 2024b), as required to erase the ordered orbital angular momentum.

Based on the distribution of ellipticities in galaxies deemed, from visual inspection, to be dE rather than dS0 or Im, it was reported (Sandage & Shaw 1980; Sandage et al. 1985) that they are not disks but rather true elliptical systems. This view has been pervasive but was partly challenged by Ryden & Terndrup (1994), who reported a greater flattening than previously recognised. Binggeli & Popescu (1995) subsequently reported consistency among the ellipticity distributions of normal (non-nucleated) dEs, dS0s, late spirals (Sdm - Sms), smooth irregulars (Im)s, and clumpy irregulars (Blue Compact Dwarfs) and a different distribution for nucleated dwarfs and a sample of giant ETGs containing ordinary S0 and E galaxies. Given how the prevalence of discs — by which it is meant a substantial rotating component — was missed in the ordinary HSB ETGs for decades, it would not be surprising if they are still missed in the LSB galaxies. As with some ordinary ETGs, some LSB dwarf ETGs reveal their disc nature by displaying bars or spiral patterns (e.g. Jerjen et al. 2000; Barazza et al. 2002; Graham et al. 2003). Initially considered something of a novelty, the significance of these discoveries went somewhat over-looked as it was not appreciated how widespread the dS0 rather than dE population was, although, at that time, it was starting to be discovered that rotation in dwarf ETGs is common (Pedraz et al. 2002; Geha et al. 2003; Toloba et al. 2009). Another reason why (some) UDGs are likely to be disc-like rather than spheroidal is that the internal stellar luminosity density profile derived by deprojecting the Sérsic $R^{1/n}$ model leads to spheroids with holes in the middle if $n < 0.5$.

Given the declining bulge-to-disc stellar-mass ratio in ETGs with declining bulge stellar masses down to at least $2 \times 10^9 M_\odot$ ($\mathcal{M}_B \approx -16$ mag; Graham 2023, his Figure A2), the continuity in the structural scaling relations shown here implies that UDGs might also be disc-like galaxies. Indeed, IC 3475 has a faint bar-like structure (Vigroux et al. 1986; Knezek et al. 1999) and H_I rotation ($W_{20} = 114 \text{ km s}^{-1}$; Huchtmeier & Richter 1989), revealing its possible disc nature.^h These latter two studies struggled to identify what IC 3475 might have evolved from, rejecting the proposition that it is a disc-stripped dwarf spiral galaxy.

The rather common IC 3475 types (Reaves 1983) may include dS0 galaxies with some knotty regions, with some displaying mild irregularities without apparent dust lanes or spiral structure. Once the irregularities and knots disperse or settle to the galaxy centre via dynamical friction — such sinking is more efficient in the brighter dwarf galaxies with their higher- n light profile and thus steeper gravitational potentials within R_e (Terzić & Graham 2005) — they will resemble the so-called dE or nucleated dE,N systems. These need not be flat discs but thick (hot) discs that are somewhat rotationally supported structures, like the HSB ETGs, with exponential-like light profiles.

^g $\mathcal{M}_B > -20$ mag, $H_0 = 50 \text{ km s}^{-1} \text{ Mpc}^{-1}$.

^hThe bar brightens the reported B -band central surface brightness to $23.3 \text{ mag arcsec}^{-2}$.

4.3. Further musings

Explanations, whether through simulations or not, for the $\mathcal{M}-\mu_0$ and $\mathcal{M}-\log(n)$ relations for ETGs would be welcome. For the low- n , faint central surface brightness ETGs, including UDGs, it is assumed here that they are primordial rather than a transformed population. Thus, they are thought to have formed along the $\mathcal{M}_B-\mu_{0,B}$ and $\mathcal{M}_B-\log(n)$ relations, with secondary processes (along with measurement error and disc inclination effects) introducing scatter to these relations and spiral formation taking them off it, as per the ‘Triangal’ evolutionary schema (Graham 2023) before major mergers return them to it. The S0 galaxies may evolve into spiral galaxies if sufficient fuel is available and able to form stars, or they may stay as they are if their HI gas disc is either stable or has been removed. The scarcity of dS galaxies suggests that this phenomenon is more common in the HSB galaxies. This scenario is supported by the distribution of galaxy types in (black hole)-bulge mass scaling diagrams (Graham 2023) due to the way bulges and black holes monotonically grow in mass, modulo the creation of UCDs through threshing (Bekki et al. 2001). Curiously, modelling spiral galaxies with a single Sérsic function reveals a distribution of Sérsic indices that peaks at $n < 1$ (Driver et al. 2006), revealing that discs do not all have exponential ($n = 1$) light profiles. Recently, Graham (2024b) has revealed how galaxy mergers have led to the anti-truncation of discs in dust-rich merger-built S0 galaxies and, more generally, to the Sérsicification of massive ETGs. The extended nature of high- n galaxy light profiles at large radii is explained by the superposition of acquired progenitor galaxy ‘discs’ and the accumulation of accreted material at large radii. These ‘discs’ are not necessarily overly flattened systems but rather the ‘disc’ component of galaxies seen in image decompositions and supported by kinematic maps showing a galaxy’s substantial rotation. Repeated galaxy mergers build a central pressure-supported spheroidal stellar system, and the dominance of a single ordered oblate structure/disc (Rong et al. 2020) is whittled away by collisions that likely have different orientations.

Acknowledgements

This paper is dedicated to Ena (née McKenzie) Graham (1931–2019), who adopted AWG long ago and graciously let him claim Scrabble victories during her multiple surgeries and lengthy hospital stays from 2017 to 2019. AWG is grateful to the Department of Astronomy at the University of Florida, Gainesville, USA, where he largely completed the figures during 2019. The delayed write-up has benefitted from an expanded UDG data set and updated entries in the figures. Publication costs were funded through the Australian and New Zealand Institutions (Council of Australian University Librarians affiliated) Open Access Agreement. This research has used the NASA/IPAC Extragalactic Database (NED) and the SAO/NASA Astrophysics Data System (ADS) bibliographic services.

References

Amorisco N. C., Loeb A., 2016, *MNRAS*, **459**, L51
 Barazza F. D., Binggeli B., Jerjen H., 2002, *A&A*, **391**, 823
 Bekki K., Couch W. J., Drinkwater M. J., 2001, *ApJ*, **552**, L105
 Bell E. F., de Jong R. S., 2001, *ApJ*, **550**, 212
 Binggeli B., Cameron L. M., 1993, *A&AS*, **98**, 297
 Binggeli B., Jerjen H., 1998, *A&A*, **333**, 17
 Binggeli B., Popescu C. C., 1995, *A&A*, **298**, 63
 Binggeli B., Sandage A., Tammann G. A., 1985, *AJ*, **90**, 1681
 Bonfini P., Dullo B. T., Graham A. W., 2015, *ApJ*, **807**, 136

Buzzo M. L., et al., 2022, *MNRAS*, **517**, 2231
 Buzzo M. L., et al., 2024, *MNRAS*, **529**, 3210
 Buzzo M. L., et al., 2025, *MNRAS*, **536**, 2536
 Caon N., Capaccioli M., D’Onofrio M., 1993, *MNRAS*, **265**, 1013
 Capaccioli M., 1989, in Corwin Jr. H. G., Bottinelli L., eds, *World of Galaxies* (Le Monde des Galaxies). pp 208–227
 Capaccioli M., 1990, in Jarvis B. J., Terndrup D. M., eds, *European Southern Observatory Conference and Workshop Proceedings Vol. 35, European Southern Observatory Conference and Workshop Proceedings*. p. 231
 Conselice C. J., 2018, *Research Notes of the American Astronomical Society*, **2**, 43
 Davies R. L., Efstathiou G., Fall S. M., Illingworth G., Schechter P. L., 1983, *ApJ*, **266**, 41
 Dekel A., Silk J., 1986, *ApJ*, **303**, 39
 Di Cintio A., Brook C. B., Dutton A. A., Macciò A. V., Obreja A., Dekel A., 2017, *MNRAS*, **466**, L1
 Driver S. P., et al., 2006, *MNRAS*, **368**, 414
 Emsellem E., et al., 2011, *MNRAS*, **414**, 888
 Errani R., Penarrubia J., Tormen G., 2015, *MNRAS*, **449**, L46
 Faber S. M., et al., 1997, *AJ*, **114**, 1771
 Fisher J. R., Tully R. B., 1975, *A&A*, **44**, 151
 Forbes D. A., Gannon J., 2024, *MNRAS*, **528**, 608
 Forbes D. A., Lasky P., Graham A. W., Spitler L., 2008, *MNRAS*, **389**, 1924
 Geha M., Guhathakurta P., van der Marel R. P., 2003, *AJ*, **126**, 1794
 Goerdt T., Moore B., Read J. I., Stadel J., 2010, *ApJ*, **725**, 1707
 Graham A. W., 2013, in Oswalt T. D., Keel W. C., eds, , Vol. 6, *Planets, Stars and Stellar Systems. Volume 6: Extragalactic Astronomy and Cosmology*. Springer Science+Business Media, Dordrecht, pp 91–140, doi:10.1007/978-94-007-5609-0-2
 Graham A. W., 2019, *Publ. Astron. Soc. Australia*, **36**, e035
 Graham A. W., 2023, *MNRAS*, **522**, 3588
 Graham A. W., 2024a, *MNRAS*, **531**, 230
 Graham A. W., 2024b, *MNRAS*, **535**, 299
 Graham A. W., Driver S. P., 2005, *Publ. Astron. Soc. Australia*, **22**, 118
 Graham A. W., Guzmán R., 2003, *AJ*, **125**, 2936
 Graham A. W., Sahu N., 2023, *MNRAS*, **520**, 1975
 Graham A. W., Worley C. C., 2008, *MNRAS*, **388**, 1708
 Graham A. W., Colless M. M., Busarello G., Zaggia S., Longo G., 1998, *A&AS*, **133**, 325
 Graham A. W., Trujillo I., Caon N., 2001, *AJ*, **122**, 1707
 Graham A. W., Jerjen H., Guzmán R., 2003, *AJ*, **126**, 1787
 Graham A. W., Merritt D., Moore B., Diemand J., Terzić B., 2006, *AJ*, **132**, 2711
 Häußler B., et al., 2013, *MNRAS*, **430**, 330
 Huchtmeier W. K., Richter O. G., 1989, *A&A*, **210**, 1
 Janz J., Penny S. J., Graham A. W., Forbes D. A., Davies R. L., 2017, *MNRAS*, **468**, 2850
 Jerjen H., Kalnajs A., Binggeli B., 2000, *A&A*, **358**, 845
 Jester S., et al., 2005, *AJ*, **130**, 873
 Jordi K., Grebel E. K., Ammon K., 2006, *A&A*, **460**, 339
 Kelvin L. S., et al., 2012, *MNRAS*, **421**, 1007
 Kennedy R., et al., 2016a, *MNRAS*, **460**, 3458
 Kennedy R., Bamford S. P., Häußler B., Brough S., Holwerda B., Hopkins A. M., Vika M., Vulcani B., 2016b, *A&A*, **593**, A84
 Knezek P. M., Sembach K. R., Gallagher III J. S., 1999, *ApJ*, **514**, 119
 Koda J., Yagi M., Yamanoi H., Komiyama Y., 2015, *ApJ*, **807**, L2
 Kormendy J., 1985, *ApJ*, **295**, 73
 Krajnović D., et al., 2013, *MNRAS*, **432**, 1768
 Marleau F. R., et al., 2024, *A&A*, **690**, A339
 Moore B., Katz N., Lake G., Dressler A., Oemler A., 1996, *Nature*, **379**, 613
 Pedraz S., Gorgas J., Cardiel N., Sánchez-Blázquez P., Guzmán R., 2002, *MNRAS*, **332**, L59
 Reaves G., 1956, *AJ*, **61**, 69
 Reaves G., 1983, *ApJS*, **53**, 375
 Rix H.-W., White S. D. M., 1990, *ApJ*, **362**, 52
 Rong Y., et al., 2020, *ApJ*, **899**, 78
 Ryden B. S., Terndrup D. M., 1994, *ApJ*, **425**, 43
 Saito M., 1979, *PASJ*, **31**, 193

- Sandage A., Binggeli B., 1984, *AJ*, **89**, 919
- Sandage A., Shaw R., 1980, Year Book 79. Year Book - Carnegie Institution of Washington Vol. 79, Washington, D.C., Carnegie Institution of Washington, <https://archive.org/details/yearbookcarne79197980cam/page/2/mode/2up>
- Sandage A., Binggeli B., Tammann G. A., 1985, pp 239–293
- Schombert J. M., McGaugh S., 2014, *Publ. Astron. Soc. Australia*, **31**, e011
- Seigar M. S., Graham A. W., Jerjen H., 2007, *MNRAS*, **378**, 1575
- Sersic J. L., 1968a, Atlas de Galaxias Australes. Observatorio Astronomico, Cordoba, Argentina
- Sérsic J. L., 1968b, Bulletin of the Astronomical Institutes of Czechoslovakia, **19**, 105
- Shull J. M., 2014, *ApJ*, **784**, 142
- Spitler L. R., Forbes D. A., 2009, *MNRAS*, **392**, L1
- Stiavelli M., Miller B. W., Ferguson H. C., Mack J., Whitmore B. C., Lotz J. M., 2001, *AJ*, **121**, 1385
- Sung E.-C., Han C., Ryden B. S., Patterson R. J., Chun M.-S., Kim H.-I., Lee W.-B., Kim D.-J., 1998, *ApJ*, **505**, 199
- Terzić B., Graham A. W., 2005, *MNRAS*, **362**, 197
- Toloba E., et al., 2009, *ApJ*, **707**, L17
- Toloba E., et al., 2014, *ApJS*, **215**, 17
- Trujillo I., Graham A. W., Caon N., 2001, *MNRAS*, **326**, 869
- Vader J. P., 1986, *ApJ*, **305**, 669
- Vigroux L., Thuan T. X., Vader J. P., Lachize-Rey M., 1986, *AJ*, **91**, 70
- de Vaucouleurs G., de Vaucouleurs A., 1972, *Mem. RAS*, **77**, 1
- van Dokkum P. G., Abraham R., Merritt A., Zhang J., Geha M., Conroy C., 2015, *ApJ*, **798**, L45
- van den Bergh S., 1990, *ApJ*, **348**, 57